FRONTIERS OF PHYSICS

RESEARCH ARTICLE
Volume 18 / Issue 4 / 43302 / 2023

Interlayer interaction mechanism and its regulation on optical properties of bilayer SiCNSs

Shuang-Shuang Kong (孔双双)[1], Wei-Kai Liu (刘卫凯)[1], Xiao-Xia Yu (于晓霞)[2], Ya-Lin Li (李亚林)[1], Liu-Zhu Yang (杨留柱)[1], Yun Ma (马昀)[1], Xiao-Yong Fang (房晓勇)[1,†]

1 Key Laboratory for Microstructural Material Physics of Hebei Province, School of Science, Yanshan University, Qinhuangdao 066004, China
2 School of Mechanical Engineering, Yanshan University, Qinhuangdao 066004, China
Corresponding author. E-mail: †fang@ysu.edu.cn
Received December 1, 2022; accepted January 9, 2023

ABSTRACT

Silicon carbide nanosheets (SiCNSs) have a very broad application prospect in the field of new two-dimensional (2D) materials. In this paper, the interlayer interaction mechanism of bilayer SiCNSs (BL-SiCNSs) and its effect on optical properties are studied by first principles. Taking the charge and dipole moment of the layers as parameters, an interlayer coupling model is constructed which is more convenient to control the photoelectric properties. The results show that the stronger the interlayer coupling, the smaller the band gap of BL-SiCNSs. The interlayer coupling also changes the number of absorption peaks and causes the red or blue shift of absorption peaks. The strong interlayer coupling can produce obvious dispersion and regulate the optical transmission properties. The larger the interlayer distance, the smaller the permittivity in the vertical direction. However, the permittivity of the parallel direction is negative in the range of 150-300 nm, showing obvious metallicity. It is expected that the results will provide a meaningful theoretical basis for further study of SiCNSs optoelectronic devices.

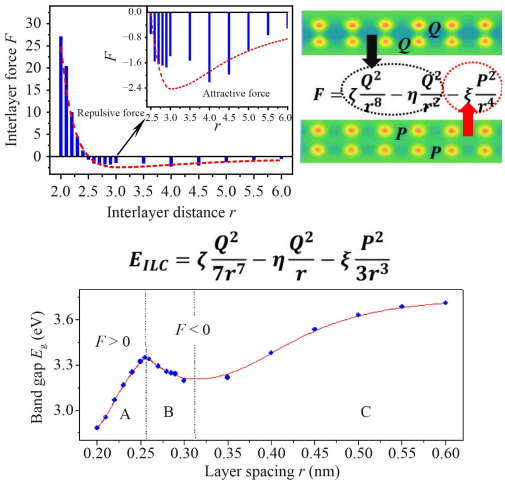

Keywords SiC nanosheets, bilayer nanosheets, interlayer coupling model, bandgap structure, optical properties

1 Introduction

Silicon carbide (SiC) materials have stable electronic properties and high thermal conductivity [1–4] and are considered suitable candidate materials for the electronics manufacturing and sensors in high power and high temperature harsh environments, with better prospects for applications in light-emitting devices and light detectors [5–7]. For a long time, much more reports about SiC nanomaterials are reported, such as nanowires [8–13] and nanotubes [14–18], especially the research on nanoribbon and nanosheets with layered structures, which have attracted widespread attention [19–23].

In 2012, Lin [24] reported the exfoliation of SiC nanosheets (SiCNSs) with a thickness of 0.5–1.5 nm, which has excellent luminescence properties. Since then, reports of SiCNSs have gradually increased, for example, due to the advantages of SiCNSs structure, the rapid electron transfer rate in SiC semiconductors, and the electrons donor effect of electrons, Sun *et al.* [25] prepared an impedance non-oxide humidity sensor based on SiCNSs, which has good humidity sensing performance. Houmada *et al.* [26] investigated the electronic and optical properties of silicon carbide nanosheets (two-

https://doi.org/10.1007/s11467-023-1263-9

dimensional monolayers) using the full potential linearization enhanced plane wave (FP-LAPW) method and the generalized gradient approximation (GGA) method in the WIEN2k package. The properties of monolayer and bilayer SiCNSs are highly dependent on their physical thickness and geometric configuration, and the optical conductivity of multilayer SiCNSs is sensitive to the interlayer distance [27]. The ultrathin SiCNSs are expected to be electrode materials for high performance supercapacitors [28] and can also be used as a load substrate to form a novel Pt SAs@SnO_2NRs@SiCNSs multi-heterojunction, providing new ways for designing new gas-sensitive materials [29]. In 2023, Liu *et al.* [30] studied the effect of the number of layers on the electronic and optical properties of few-layer SiCNSs (FL-SiCNSs) which showed that the more the layer number, the stronger the interlayer coupling and the smaller the band gap of FL-SiCNSs.

The above literature reports show that the theoretical studies of 2D SiC mostly focus on the electrical, magnetic and optical properties of monolayer SiCNSs (ML-SiCNSs), few-layer SiCNSs (FL-SiCNSs) and ultrathin SiCNSs, while the study on the effect of interlayer coupling mechanism on the photoelectric properties of multilayer SiCNSs is few. So far, there have been some reports showing the effect of interlayer or interwall interactions on the photoelectric properties of multilayer or multiwall nanostructures [31–35]. In this paper, the interlayer coupling mechanism of BL-SiCNSs is studied systematically, and the interlayer coupling model is established in which the interlayer force is related to the positive charge of SiCNSs, but mainly to the electric dipole moment of SiCNSs. On this basis, the effects of different layer spacing on the band gap and optical properties of BL-SiCNSs are analyzed, and the regulation of interlayer coupling on the optical properties of BL-SiCNSs is discussed. Since the charges and dipole moments of the layers can be easily obtained from the experimental and lattice structures, the modulation of the band gap and optical properties of the SiCNSs is easier to achieve in this model.

2 Theory and model

2.1 Bilayer SiCNSs model

In order to facilitate the wide range change of interlayer distance, the 2H-SiC unit cell is translated three cycles in the a and b directions, respectively, to construct a large $4 \times 4 \times 4$ supercell. On this supercell, the c axis is sheared to obtain ML- and BL-SiCNSs models with different interlayer distances, each layer has 32 carbon atoms and 32 silicon atoms, respectively, as shown in Fig. 1. Among them, the BL-SiCNSs choose AB-type stacking and cut out the interlayer covalent bonds.

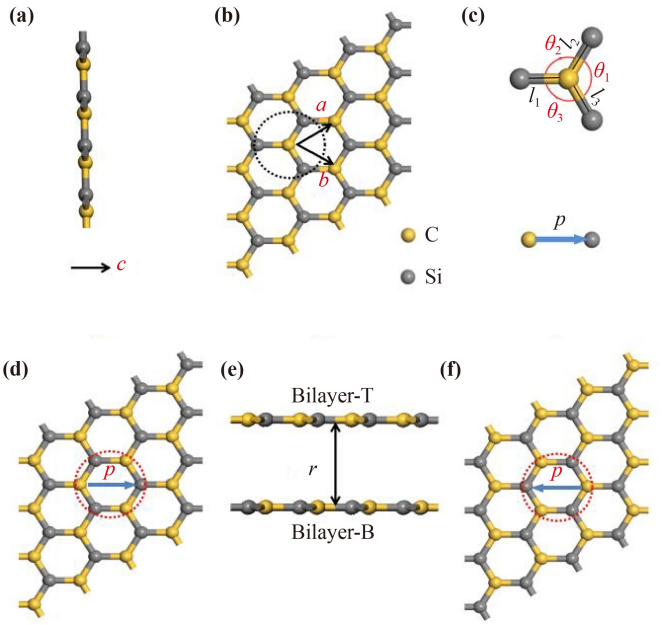

Fig. 1 Structural models of monolayer and bilayer SiCNSs. **(a)** Side view, **(b)** lattice structure, and **(c)** equivalent dipole of an ML-SiCNSs, **(e)** BL-SiCNSs, **(d)** and **(f)** are the bilayer-T and bilayer-B lattice structures.

Change the interlayer distance r to perform first-principles calculations for BL-SiCNSs with $r = 0.2$–0.6 nm, respectively. In order to avoid the influence of other SiCNSs, a 15 Å vacuum layer is added to the outer side of ML- and BL-SiCNSs [30].

In this paper, the SiCNSs model was calculated by the CASTEP module of Material Studio. The exchange-correlation can be calculated using the generalized gradient approximation (GGA) PBE method [36] and add dispersion correction [37]. According to the previous optimization test, set the plane wave cutoff energy to 500 eV and the K grid point to $5 \times 5 \times 2$. Set the necessary convergence criteria: the convergence criterion for the interaction forces between atoms is set to 0.01 eV/Å; the convergence criterion for single atomic energy is set to 2×10^{-5} eV; the convergence standard for stress in the structure is set to 0.01 GPa, and the maximum atom displacement convergence standard is set to 0.002 Å. For van der Waals correction, the semi-empirical dispersion correction based on the Tkatchenko and Scheffler (TS) scheme was used in the calculations [30]. When all four values reach the convergence criterion, the model structure reaches the most stable state. Considering that the band gap value calculated by Material studio is underestimated, the choice of scissor operator is 1.002 eV based on Ref. [24] of 2H-SiC and SiCNSs and the previous calculations of this study. The scissor operation only affects the position of the absorption peak and has little effect on the absorption peak.

2.2 Interlayer binding energies and interaction forces

The heat released when multiple isolated atoms combine into crystals is called binding energy (or cohesion) [18]. The ML-SiCNSs' binding energy can be expressed as

$$E_B^{ML} = E_T^{ML} - N_{\mathrm{Si}}\mu_{\mathrm{Si}} - N_{\mathrm{C}}\mu_{\mathrm{C}}, \quad (1)$$

where E_T^{ML} is the total energy of ML-SiCNSs, μ_{Si}, μ_{C} are the energy (chemical potential) of isolated Si and C atoms, and N_{Si}, N_{C} are the number of Si and C atoms. A negative E_B^{ML} value indicates heat release, and a larger absolute value indicates that the lattice structure is more stable. Similarly, the BL-SiCNSs' binding energy can also be written as

$$E_B^{BL} = E_T^{BL} - 2N_{\mathrm{Si}}\mu_{\mathrm{Si}} - 2N_{\mathrm{C}}\mu_{\mathrm{C}}, \quad (2)$$

where E_T^{BL} is the total energy of BL-SiCNSs.

A BL-SiCNSs can be seen as formed by two ML-SiCNSs, so the interaction energy between the two layers can be expressed as [30]

$$E_{ILC} = E_B^{BL} - 2E_B^{ML}. \quad (3)$$

The formation energy [13] can usually be used to represent the absorption/release heat relationship of this process, i.e.,

$$E_F = E_T^{BL} - 2E_T^{ML} = E_{ILC}. \quad (4)$$

A negative value for formation energy indicates that heat is released when BL-SiCNSs are formed, and a positive value indicates heat absorption. Obviously, the larger the negative value or the smaller the positive value, the easier it is to implement for bilayer SiCNSs [38]. According to the relationship between the conservative force and the associated potential energy, the interlayer interaction force can be written as [39]

$$\boldsymbol{F} = -\frac{\partial E_{ILC}}{\partial r}, \quad (5)$$

where r is the interlayer distance of BL-SiCNSs. In this paper, BL-SiCNSs' interlayer interaction energy is referred to as interlayer coupling energy.

3 Results and discussion

3.1 Interlayer coupling mechanism

3.1.1 Optimization results from first principles

The optimized structural parameters of ML- and BL-SiCNSs are shown in Table 1, where bilayer-T and bilayer-B represent the top and bottom of BL-SiCNSs, atomic positions, corresponding bond lengths, and bond angles are shown in Fig. 1.

As shown in Fig. 1 and Table 1, the ML-SiCNSs is hexagonal honeycomb structure. Since the electronegativity of Si is smaller than that of C, the Si-C bond presents a polar covalent bond, so it will form a molecular dipole. For a honeycomb structure with regular distribution, the dipole moments of adjacent hexagons inside cancel each other, but the dipole moments at the edges do not cancel. Therefore, the finitely large ML-SiCNSs can be regarded as an equivalent electric dipole, whose dipole moment P can be obtained from Table S1, and its value is shown in Table 1. For BL-SiCNSs, in addition to atomic charges, both bilayer-T and bilayer-B have similar structures to ML-SiCNSs. Their dipole moments can also be obtained according to Tables S2 and S3, as shown in Table 1. Because the position of Si and C are opposite in the two layers, bilayer-T and bilayer-B form a pair of electric dipoles with opposite polarity, as shown in Fig. 1.

Since bilayer-T and bilayer-B have the same bond length and bond angle as the ML-SiCNSs, their total bond energy is also the same. Therefore, the binding energies of bilayer-T and bilayer-B are the same as those of ML-SiCNSs, and their values are shown in Table 2, where Q is the total positive/negative charge of bilayer-T or bilayer-B, and P is the total dipole moment of bilayer-T or bilayer-B. In Table 2, the binding energy and formation energy of different interlayer distance are calculated by Eqs. (1)–(4). The negative value of the binding energy indicates that the BL-SiCNSs with interlayer distance between 0.2 and 0.6 nm can form a stable structure. Among them, the most stable structure needs to be determined by interlayer forces.

3.1.2 Interlayer force model and coupling mechanism

The interlayer coupling energy and the interaction force of the BL-SiCNSs at different interlayer distance can be obtained by Eqs. (3) and (5), as shown in Fig. 2.

It can be seen that when the interlayer distance between the bilayer-T and bilayer-B layers is less than 0.24 nm, the interlayer force is positive, indicating that the repulsive force plays a major role. When the interlayer distance is greater than or equal to 0.25 nm, the interlayer force is negative, indicating the dominant role of the

Table 1 Structural parameters of ML- and BL-SiCNSs.

Structure	Supercell constants		Atomic charge (Mulliken)		Bond length (Å)			Bond angle (°)			Dipole moment
	$a = b$ (Å)	Γ (°)	Si(e)	C(e)	l_1	l_2	l_3	θ_1	θ_2	θ_3	P (eÅ)
Monolayer	12.3	120	+1.46	–1.46	1.78	1.78	1.78	120	120	120	25.67
Bilayer-T	12.3	120	+1.44	–1.44	1.78	1.78	1.78	120	120	120	23.66
Bilayer-B	12.3	120	+1.44	–1.44	1.78	1.78	1.78	120	120	120	–23.67

Table 2 Binding energy and charge distribution of ML- and BL-SiCNSs.

SiCNSs	Distance r (Å)	Binding energy (eV)	Formation energy (eV)	Charge $\pm$ Q (e)	Dipole P (eÅ)	Distance r (Å)	Binding energy (eV)	Formation energy (eV)	Charge $\pm$ Q (e)	Dipole P (eÅ)
Monolayer	0	–266.655	–	23.36	25.67	2.8	–462.160	–8.850	23.04	23.66
Bilayer	2.0	–457.663	–4.353	23.84	24.48	2.9	–461.980	–8.670	23.04	23.66
	2.1	–460.370	–7.060	23.68	24.32	3.0	–461.812	–8.502	23.04	23.66
	2.2	–461.738	–8.429	23.52	24.15	3.5	–461.264	–7.954	23.04	23.66
	2.3	–462.363	–9.054	23.36	23.99	4.0	–460.284	–6.974	23.04	23.66
	2.4	–462.624	–9.315	23.36	23.99	4.5	–459.052	–5.742	23.20	23.82
	2.5	–462.626	–9.317	23.20	23.82	5.0	–458.317	–5.007	23.20	23.82
	2.6	–462.487	–9.178	23.20	23.82	5.5	–457.851	–4.542	23.20	23.82
	2.7	–462.317	–9.008	23.20	23.82	6.0	–457.598	–4.288	23.20	23.82

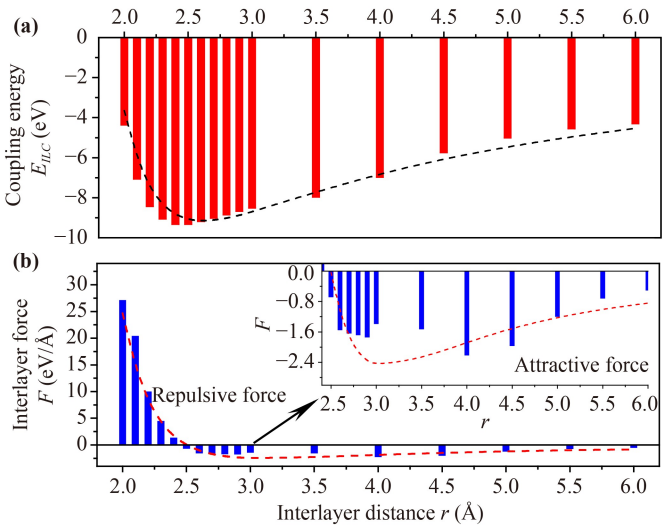

Fig. 2 Interlayer distance dependent coupling energy **(a)** and interlayer forces **(b)**.

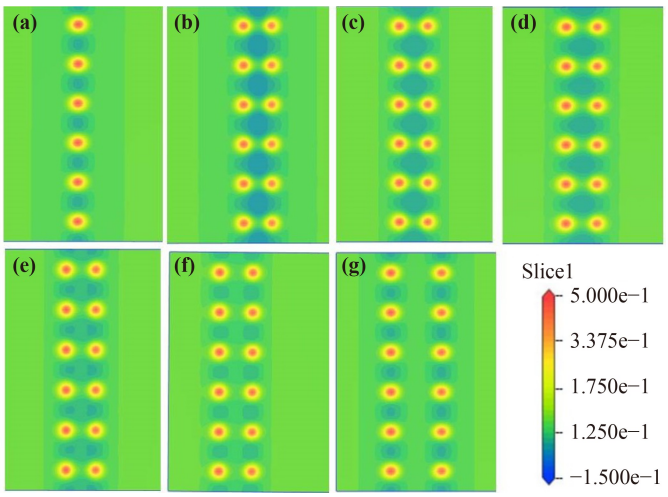

Fig. 3 Differential state density of state, **(a)** is monolayer, **(b–g)** are bilayers with distance of 2, 2.1, 2.2, 2.4, 2.8 and 4 Å respectively.

interlayer attraction. According to the coupling energy and force data of different interlayer distance (Table S4), the repulsive and attractive forces between layers are fitted, as shown in Fig. S1. Thus, the interlayer force can be set as

$$F = \frac{A}{r^8} - \frac{B}{r^2} - \frac{C}{r^4}. \tag{6}$$

According to the data in Table S4, the coefficients of the above equation (6) can be solved, then the interlayer force of BL-SiCNSs can be written as

$$F = \frac{8969}{r^8} - \frac{29}{r^2} - \frac{50}{r^4}. \tag{7}$$

Figure 3 shows the differential density of state of ML- and BL- SiCNSs. It can be seen that the Si and C atoms in each layer carry positive/negative charges respectively.

As can be seen from Table S5, a large number of antibonding occurs between layers in the range of 0.2–0.24 nm, indicating that the shielding effect of extranuclear electrons of interlayer atoms is lost. Thus, when the interlayer distance is small, the electron clouds of the two layers overlap between the layers [as shown in Figs. 1(b)–(e)], and the positive charge exposure leads to the coulomb repulsive force between the layers. In this process, there are polar covalent bonds (ionic bonds) between different layers, resulting in Coulomb attraction. As the interlayer distance increases, the overlap between the electron cloud decreases, the Coulomb attraction gradually increases until the interlayer distance reaches 0.25 nm, and the Coulomb interaction becomes the dominant mechanism. Given that the positive charge of bilayer-T and bilayer-B is Q, the repulsive force between the layers can be expressed as

$$F_r = \zeta\frac{Q^2}{r^8} - \eta\frac{Q^2}{r^2}. \tag{8}$$

As can be seen from Table S5, when the interlayer distance is between 0.25 and 0.29 nm, the interlayer

force mainly comes from the Coulombic attraction of Si and C atoms. When the interlayer distance is larger than 0.3 nm, the polar covalent bond between the layers disappears, and the attraction mainly comes from the interaction between the two equivalent dipolar layers. Assuming that the dipole moment is P, the interlayer attractive force can be expressed as

$$F_a = -\eta\frac{Q^2}{r^2} - \xi\frac{P^2}{r^4}, \tag{9}$$

where η and ξ is a constant. For this example, the three constants available from Table S4 are 0.472, 0.054 and 0.088, respectively. Based on Eqs. (5), (8) and (9), the interlayer force and coupling energy of BL-SiCNSs can be written as follows:

$$F = \zeta\frac{Q^2}{r^8} - \eta\frac{Q^2}{r^2} - \xi\frac{P^2}{r^4}, \tag{10}$$

$$E_{\mathrm{ILC}} = \zeta\frac{Q^2}{7r^7} - \eta\frac{Q^2}{r} - \xi\frac{P^2}{3r^3}. \tag{11}$$

Compared with some interlayer potentials used in graphite, such as Lennard–Jones potential [40], Mie potential [41], and Kolmogorov–Crespy potential [42, 43], the above models have clear physical images and mechanism of action. And the model parameters Q (charges of the layers) and P (dipole moments of the layers) can be easily obtained from experiments and lattice structures. Therefore, it is easier to regulate the optical and electrical properties of BL-SiCNSs.

3.2 Influence of interlayer coupling on band gap

Figure 4 shows the effect of interlayer coupling on the band structure of the bilayer SiCNSs. From Fig. 4(a), it can be seen that the conduction band bottom of the single-layer SiCNSs is at the center of the Brillouin zone (Γ point) and the valence band top is at the boundary (F point) in the [010] direction, which belongs to the indirect band gap. The energy band structure has obvious directionality, that is, the [001] direction (Γ→Z) valence band and the conduction band are gradually flattened, [010] direction (Γ→F) the conduction band and the valence band are moving in the direction of high energy, showing a curved shape. This is similar to what has been reported in other literature [39].

The energy band and state density of BL-SiCNSs at different interlayer distances are shown in Fig. S2. Similar to ML-SiCNSs, the band structure of BL-SiCNSs also exhibits the characteristics of parallel [001] direction and [010] direction curvature, and all belong to the indirect band gap, as shown in Figs. 4(b) and (c). When the layer distance is 0.6 nm, the band gap of BL-SiCNSs has a maximum value of 3.71 eV, which is smaller than band gap of ML-SiCNSs, indicating that interlayer

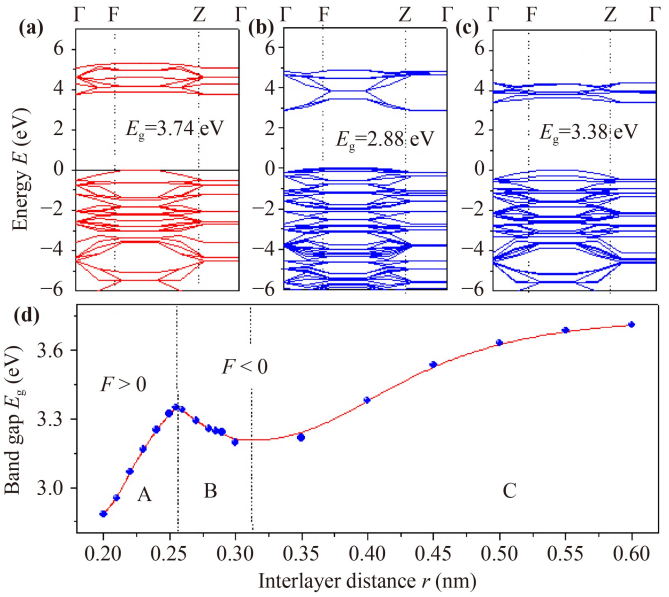

Fig. 4 Effect of interlayer coupling on band structure of SiCNSs, **(a)** ML-SiCNSs band-gap, **(b)** small (r = 0.20 nm) and **(c)** large (r = 0.40 nm) interlayer distance BL-SiCNSs band-gap, **(d)** interlayer distance dependent bandgap of SiCNSs.

coupling will reduce the band gap of BL-SiCNSs, and similar phenomena have been found in multilayer SiCNSs and MWSiCNTs [44, 35]. In order to further reveal the mechanism of interlayer coupling on the band gap of SiCNSs, Fig. 4(d) gives the relationship between the band gap of SiCNSs with the interlayer distance. It can be seen that when the interlayer distance is less than 0.25 nm, as the interlayer distance decreases, the repulsion force increases and the band gap decreases, as shown in Fig. 4(d) in area A; when the interlayer distance is greater than 0.25 nm, the layers appear to be mutually attracted. As the interlayer distance increases, the attractiveness gradually increases and the band gap gradually decreases, as shown in the B area in Fig. 4(d); when the interlayer attraction reaches the maximum (about 0.30 nm), as the interlayer distance increases, the interlayer coupling weakens, and the band gap increases and eventually tends to the monolayerr SiCNSs band gap, as shown in the C region in Fig. 4(d). Comparing Fig. 4(d) with Fig. 2(b), the stronger the interlayer coupling, the smaller the band gap of SiCNSs, and the weaker the interlayer coupling, the larger the band gap of SiCNSs. However, the band gap of the bilayer SiCNSs is not the maximum, whether the coupling energy is minimal (about 0.25 nm) or the force is zero (about 0.25 nm). Only when the layer distance is greater than 0.60 nm, that is, bilayer-T and bilayer-B are independent of each other, the band gap of the bilayer SiCNSs tends to the band gap of the monolayer SiCNSs.

3.3 Influence of interlayer coupling on photoelectric properties

3.3.1 Optical absorbability

The optical properties of semiconductor are closely related to its band structure. For SiCNSs, valence band electrons will transit to conduction band when absorbing photons $\nu > E_g/h$. The relationship between optical absorption and band gap is as following [45]:

$$(\alpha h\nu)^{1/r} = A\,(h\nu - E_g)\,, \tag{12}$$

where A is a constant and $h\nu$ is the photon energy.

Figure 5 is the absorption spectrum of BL-SiCNSs with different interlayer distances, and for the comparative analysis of the coupling mechanism between layers, Figs. 5(a, d), (b, e), (c, f) correspond to the A, B and C regions in Fig. 4(d), respectively. And the same is true in Figs. 6–10 below. As the interlayer distance increases, the interlayer repulsion of area A decreases rapidly, the attractiveness of zone B gradually increases, and the attraction of C region slowly decreases.

Along the direction of vertical SiCNSs, the wide absorption peaks in the frequency band with the decrease of repulsion force by 1500–2500 THz are divided into two, of which the low frequency peak redshifts and the peak increases significantly, and the high frequency peak blueshifts and the peak increase is small, as shown in Fig. 5(a); when entering the attraction, as the gravitational force increases, the absorption peak near 1500 THz gradually widens and splits again, and the absorption edge is redshifted. The absorption peak near 2500 THz increases with a slight blueshift, as shown in Fig. 5(b); as the interlayer distance further increases, the attraction decreases, the absorption peak of the secondary split near 1250 THz decreases rapidly, the other peak of the quadratic split (near 1750 THz) does not change significantly, while the absorption peak near 2500 THz continues to shift blue and the peak increases slightly, as shown in Fig. 5(c).

Along the parallel SiCNSs direction, there are two absorption peaks near 1200 and 2000 THz when the repulsion force is maximum, and as the repulsion weakens, both peaks undergo redshift, of which the high frequency peaks move more amplitude, resulting in the two absorption peaks tending to coincide, as shown in Fig. 5(d). In area B, as attraction increases, the trend of two absorption peaks merging increases, as shown in Fig. 5(e). After entering the area C, the attraction slowly weakens, at which point the two absorption peaks of the original split are further merged, and the peaks are enhanced, forming a stable light absorption band near 1000 THz, as shown in Fig. 5(f).

3.3.2 Photoconductivity

Under the action of light, materials will lead to electron emission, conductivity change or electric potential, and these optoelectronic properties are the basis for the development of optoelectronic devices.

Figure 6 shows the influence of layer distance on the conductivity of BL-SiCNSs. The vertical conductivity in the area A increase with the decrease of the repulsion force, and the spectral peak near 2000 THz is divided into two, moving in the direction of low frequency and high frequency, respectively. The two spectral peaks of parallel conductivity (around 1200 and 2000 THz) undergo redshift, where the high frequency peaks move more amplitudes, causing the two peaks to converge, as shown in Figs. 6(a) and (d); in the area B, as the attraction

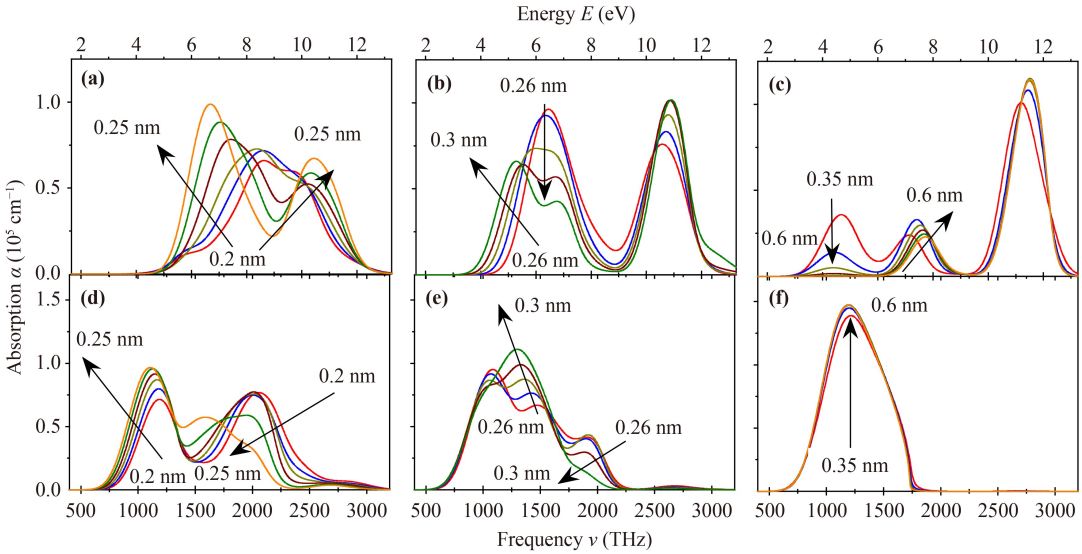

Fig. 5 Interlayer distance dependent optical absorption properties. **(a–c)** represents the absorption spectrum in the [001] direction, **(d–f)** represents the absorption spectrum in the [010] direction.

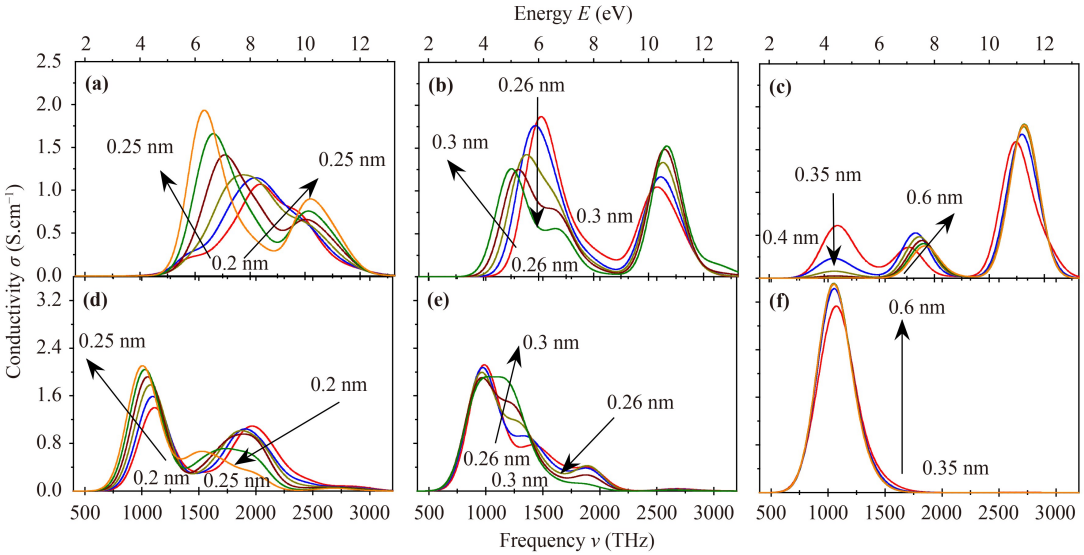

Fig. 6 Interlayer distance dependent conductivity spectrum. **(a–c)** represents the [001] direction, **(d–f)** represents the [010] direction.

increases, the vertical conductivity near 1500 THz gradually decreases and tends to split, and a significant redshift appears on the spectral edges. The vertical conductivity (around 2500 THz) split by the area A gradually increases and slowly blueshift. For parallel conductivity, the combined trend of the two high frequency peaks increases to form a wider conductivity band, as shown in Figs. 6(b) and (e); after entering the C zone, as the attraction slowly weakens, the vertical conductivity forms three stable spectral peaks around 1000 THz, 1750 THz and 2750 THz, respectively, while the parallel conductivity produces strong spectral peaks around 1000 THz, as shown in Figs. 6(c) and (f).

Comparing Figs. 5 and 6, the spectra of light absorption and conductivity are very similar: as the interlayer distance increases, three stable spectral peaks gradually appear in the vertical direction, and the peaks increase with increasing frequency. Parallel directions gradually form a stable spectral peak. Whether in the vertical or parallel direction, the peak positions corresponding to the light absorption and conductivity are almost the same, indicating that the conductivity comes from the photogenerated carrier. That is, when the bilayer SiCNSs are irradiated by light at frequencies $\nu > E_g/h$, the electrons of the valence band absorb the photon energy and jump to the conduction band, while forming a hole in the valence band. This electron and hole produced by light irradiation are called photogenerated carrier, and their directional movement forms a photocurrent, and the conductivity is called photogenerated electrical conductivity. Since the larger the light absorption, the more photogenerated carriers are generated, and the greater the conductivity, the photoconductivity spectrum is relatively like the light absorption spectrum, and they have the same variation trend. However, as the carrier concentration increases, so does the probability of electron-hole complex, resulting in a decrease in the lifetime of photogenerated carriers. Therefore, the width of the conductivity spectrum is usually smaller than the width of the absorption spectrum. The above photoconductivity features allow SiCNSs to be used in optoelectronic devices. For example, using Figs. 6(a), (b), (d) and (e) spectral characteristics, the vertical conductivity of the 120 to 310 nm band or the parallel conductivity of the 150 to 420 nm band can be adjusted; for example, Figs. 6(c) and (f) show that in the range of 200 to 410 nm, stable bilayer SiCNSs are a natural photoconductor plate, which is very suitable for the manufacture of UV-FETs [46].

3.4 Influence of interlayer coupling on optical properties

3.4.1 Refractive index and extinction coefficient

When a beam of light illuminates SiCNSs, in addition to some of the energy reflected on the surface, a part of the energy enters its interior and propagates. According to Snell's law, both reflection and refraction (transmission) behavior are closely related to the SiCNSs complex refractive index ($N = n + \mathrm{i}\kappa$). In the complex refractive index, the imaginary part (extinction coefficient) κ can be obtained from the absorption coefficient, i.e.,

$$\kappa = \frac{c}{2\omega}\alpha. \tag{13}$$

The extinction coefficient spectra of SiCNSs with different interlayer distances are shown in Fig. 7. The spectral peak position of the extinction coefficient is exactly the same as the optical absorption peak. The main difference is that as the frequency increases, the value of the

extinction coefficient spectral peak is significantly lower than the corresponding absorption peak.

The real and imaginary parts of the complex refractive index follow the Kramers–Kronig relationship, so the refractive index spectrum of the bilayer SiCNSs can be obtained from Fig. 7, as shown in Fig. 8.

From Fig. 8, the refractive index of SiCNSs with different interlayer distances is wavy in the range of 500–3200 THz, where the peak of the extinction coefficient corresponds to the middle of the adjacent peaks and valleys. The SiCNSs with the same interlayer distance, [010] the directional refractive index fluctuation amplitude is greater than the amplitude of the [001] direction. In the area A with strong interlayer coupling to the area B, the influence of the interlayer distance on the fluctuation amplitude is more obvious. In the area C with weak interlayer coupling, the interlayer distance has little effect on the swing amplitude, especially the refractive index at the [010] direction and the [001] direction 120 nm. This indicates that strong interlayer coupling produces more pronounced dispersion and can adjust the propagation behavior of light in SiCNSs.

3.4.2 Dielectric properties

The propagation behavior of light in SiCNSs stems from

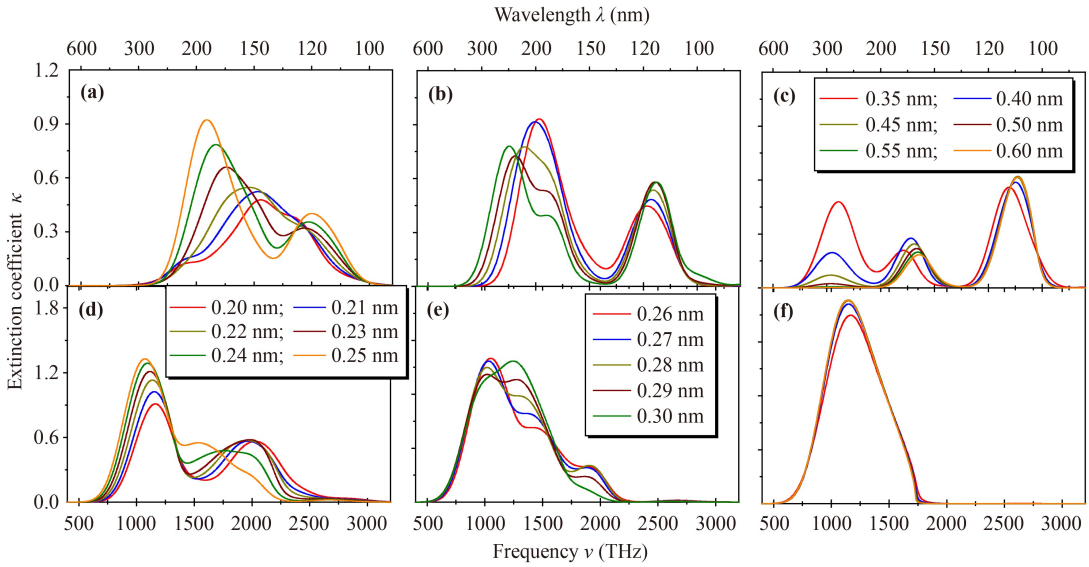

Fig. 7 Interlayer distance dependent extinction coefficient spectrum. **(a–c)** means along the [001] direction, **(d–f)** means along the [010] direction.

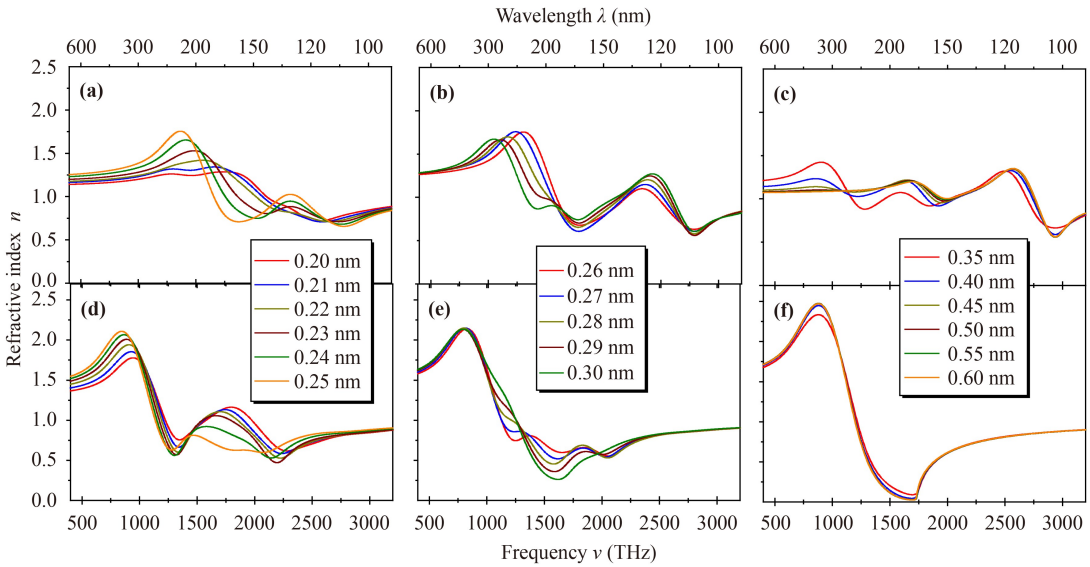

Fig. 8 Interlayer distance dependent refractive index spectrum. **(a–c)** means along the [001] direction, **(d–f)** means along the [010] direction.

particle polarization excited by alternating variable electric fields, that is, the dielectric response under electromagnetic waves. As can be seen from Ref. [47], the following simple relationship between the complex dielectric constant and the complex refractive index is satisfied:

$$n = \sqrt{\frac{\sqrt{\varepsilon'^2 + \varepsilon''^2} + \varepsilon'}{2}} \approx \sqrt{\varepsilon'}, \tag{14}$$

$$\kappa = \sqrt{\frac{\sqrt{\varepsilon'^2 + \varepsilon''^2} - \varepsilon'}{2}} \approx \frac{\varepsilon''}{2n}. \tag{15}$$

The dielectric constant of SiCNSs can be obtained, as shown in Figs. 9 and 10.

Figures 9 and 10 show that the dielectric constant of SiCNSs follows the Lorentz model, which can be expressed as a dielectric constant for multiple dielectric response [17]

$$\varepsilon'(\omega) = 1 + \frac{e^2 N}{m^* \varepsilon_0} \sum_{j=1} \frac{\omega_{j0}^2 - \omega^2}{\left(\omega_{j0}^2 - \omega^2\right)^2 + (\omega/\tau)^2}, \tag{16}$$

$$\varepsilon''(\omega) = \frac{e^2 N}{m^* \varepsilon_0} \sum_{j=1} \frac{\omega/\tau}{\left(\omega_{j0}^2 - \omega^2\right)^2 + (\omega/\tau)^2}, \tag{17}$$

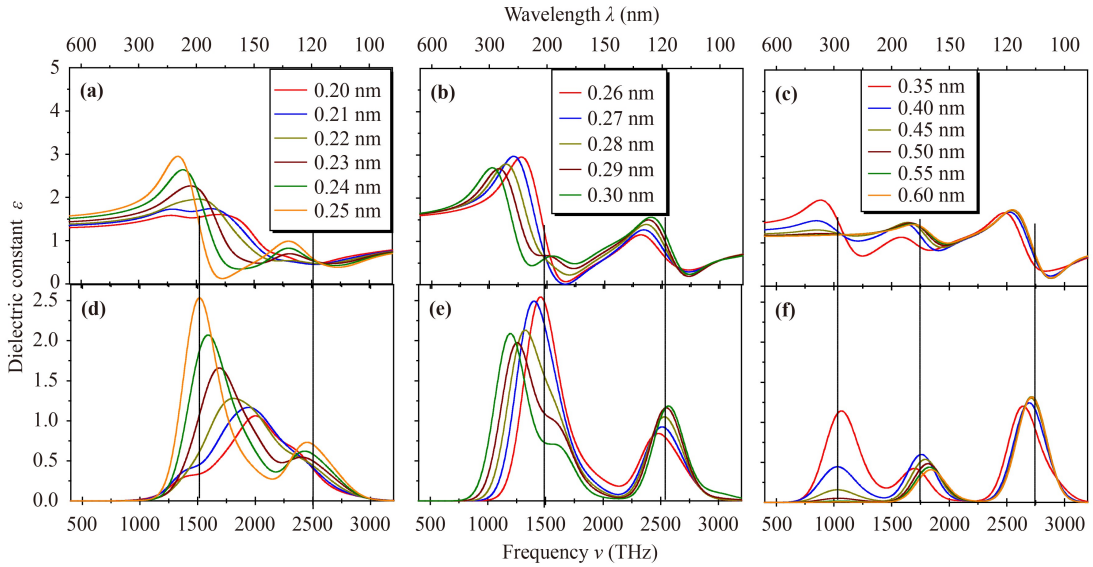

Fig. 9 Interlayer distance dependent dielectric constant on the vertical direction. **(a–c)** represents the real part of the dielectric constant, and **(d–f)** represents the imaginary part of the dielectric constant.

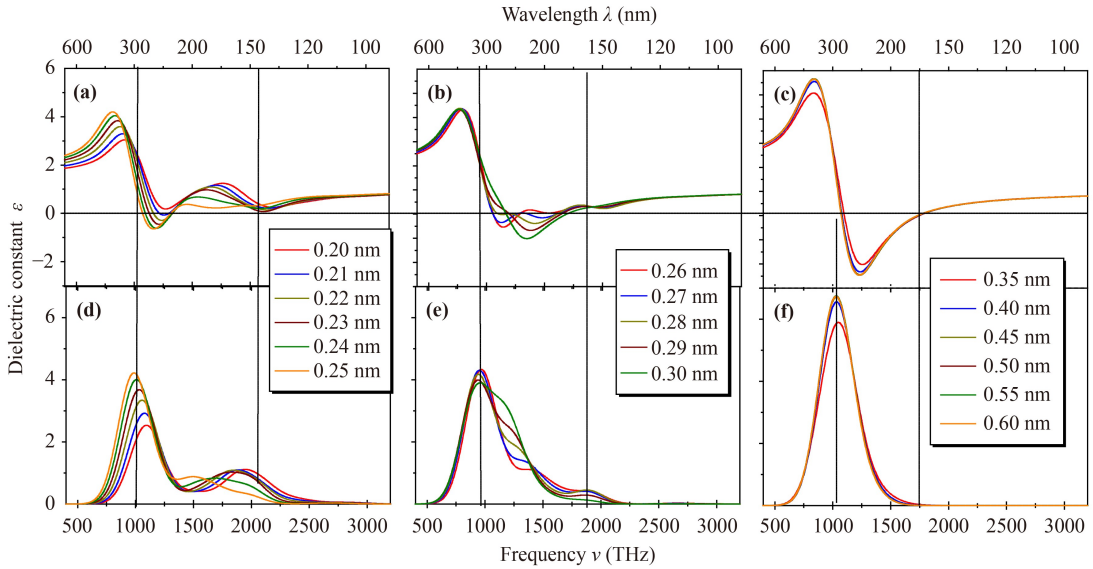

Fig. 10 Interlayer distance dependent dielectric constant on the parallel direction. **(a–c)** represents the real part of the dielectric constant, and **(d–f)** represents the imaginary part of the dielectric constant.

where N and m^* are electron concentration and effective mass respectively, τ represents the relaxation time of electron transition, and ω_{j0} represents the oscillation frequency. Specifically, there are two different mechanisms of plasma oscillation and electron displacement polarization. As can be seen from Fig. 3, when the interlayer distance is small, the two layers of electron clouds overlap between the layers, and the electrons oscillate in the vertical direction, and the larger the distance, the greater the amplitude, as shown in Fig. 9(a). As the interlayer distance increases, overlapping electron clouds disappear and accumulate in their respective molecular layers, at which point the electrons produce displacement polarization, and the larger the interlayer distance, the smaller the electron displacement polarization rate and the smaller the dielectric constant, as shown in Figs. 9(b) and (c). For the [010] direction, due to the presence of large photogenerated carriers, the dielectric response mechanism of SiCNSs is mainly derived from the plasma oscillation of these photoelectron [20, 36]. And it shows obvious metallicity in 150–300 nm band, as shown in Fig. 10.

4 Conclusion

Optimizing the data from first principles, we theoretically studied the interlayer interaction mechanism, band gap, and optical properties of bilayer SiCNSs. The results show when the interlayer distance between the bilayer-T and bilayer-B layers is less than 0.24 nm, the repulsive force plays a major role. When the interlayer distance is greater than or equal to 0.25 nm, the dominant role of the interlayer attraction. When the interlayer distance is between 0.25 and 0.29 nm, the interlayer force mainly comes from the Coulombic attraction of Si and C atoms. When the interlayer distance is larger than 0.30 nm, the attraction mainly comes from the interaction between the two equivalent dipolar layers. Interlayer coupling reduces the band gap of bilayer SiCNSs. In terms of optics, it was found that areas with strong interlayer coupling produce more pronounced dispersion. Along the vertical SiCNSs direction, the wide absorption peaks in the 1500–2500 THz band are divided into two with the reduction of repulsion, of which the low frequency peaks are redshifted and the peaks are increased significantly, and the high frequency peaks are blue shift and the peak increase is small; when entering the attraction action, the absorption peak gradually widens and splits again with the increase of gravity, and the absorption edge is redshifted; as the interlayer distance increases further and the attraction decreases, the absorption peak of the quadratic split near 1250 THz decreases rapidly, the other peak of the quadratic split (near 1750 THz) does not change significantly, while the absorption peak near 2500 THz continues to blueshift and the peak increases slightly. Along the parallel SiCNSs direction, the overall trend is the process of absorption peak merger. The spectral peak position of the conductivity and extinction coefficient is exactly as same as the optical absorption peak, the main difference is that the width of the conductivity spectrum is usually smaller than the width of the absorption spectrum. As the frequency increases, the value of the extinction coefficient spectral peak is significantly lower than the corresponding absorption peak.

Electronic supplementary materials The online version contains supplementary material available at https://doi.org/10.1007/10.1007/s11467-023-1263-9 and https://journal.hep.com.cn/fop/EN/10.1007/s11467-023-1263-9.

Acknowledgements This work was supported by Hebei Natural Science Foundation (Grant No. A2021203030) and the National Natural Science Foundation of China (Grant No. 11574261).

References

1. J. J. Wang, X. Y. Fang, G. Y. Feng, W. L. Song, Z. L. Hou, H. B. Jin, J. Yuan, and M. S. Cao, Scattering mechanisms and anomalous conductivity of heavily N-doped 3C-SiC in ultraviolet region, *Phys. Lett. A* 374(22), 2286 (2010)
2. X. L. Feng, M. H. Matheny, C. A. Zorman, M. Mehregany, and M. L. Roukes, Low voltage nanoelectromechanical switches based on silicon carbide nanowires, *Nano Lett.* 10(8), 2891 (2010)
3. X. Y. Fang, K. Wang, Z. L. Hou, H. B. Jin, Y. Q. Li, and M. S. Cao, Electronic scattering leads to anomalous thermal conductivity of n-type cubic silicon carbide in the high-temperature region, *J. Phys. :Condens. Matter* 24(44), 445802 (2012)
4. R. Maboudian, C. Carraro, D. G. Senesky, and C. S. Roper, Advances in silicon carbide science and technology at the micro- and nanoscales, *J. Vac. Sci. Technol. A* 31(5), 050805 (2013)
5. H. Okumura, A roadmap for future wide bandgap semiconductor power electronics, *MRS Bull.* 40(5), 439 (2015)
6. B. Whitaker, A. Barkley, Z. Cole, B. Passmore, D. Martin, T. R. McNutt, A. B. Lostetter, J. S. Lee, and K. Shiozaki, A high-density, high-efficiency, isolated on-board vehicle battery charger utilizing silicon carbide power devices, *IEEE Trans. Power Electron.* 29(5), 2606 (2014)
7. H. Ou, Y. Ou, A. Argyraki, S. Schimmel, M. Kaiser, P. Wellmann, M. K. Linnarsson, V. Jokubavicius, J. Sun, R. Liljedahl, and M. Syväjärvi, Advances in wide bandgap SiC for optoelectronics, *Eur. Phys. J. B* 87(3), 58 (2014)
8. G. Cheng, T. H. Chang, Q. Qin, H. Huang, and Y. Zhu, Mechanical properties of silicon carbide nanowires: effect of size-dependent defect density, *Nano Lett.* 14(2), 754 (2014)

9. M. Awais, H. Mousa, and K. Teker, Effect of pH on transport characteristics of silicon carbide nanowire field-effect transistor (SiCNW-FET), *J. Mater. Sci. Mater. Electron.* 32(3), 3431 (2021)
10. X. Zhang, J. Wang, Z. Yang, X. Tang, and Y. Yue, Strong structural occupation ratio effect on mechanical properties of silicon carbide nanowires, *Sci. Rep.* 10(1), 11386 (2020)
11. S. Li, J. Li, Q. Su, X. Liu, H. Zhao, and M. Ding, Enhanced n-type conductivity of 6H-SiC nanowires by nitrogen doping, *Micro & Nano Lett.* 14(9), 999 (2019)
12. H. Gao, H. Wang, M. Niu, L. Su, X. Fan, J. Wen, and Y. Wei, Oxidation simulation study of silicon carbide nanowires: A carbon-rich interface state, *Appl. Surf. Sci.* 493, 882 (2019)
13. Y. H. Jia, P. Gong, S. L. Li, W. D. Ma, X. Y. Fang, Y. Y. Yang, and M. S. Cao, Effects of hydroxyl groups and hydrogen passivation on the structure, electrical and optical properties of silicon carbide nanowires, *Phys. Lett. A* 384(4), 126106 (2020)
14. P. Nematollahi and M. D. Esrafili, A DFT study on the N_2O reduction by CO molecule over silicon carbide nanotubes and nanosheets, *RSC Adv.* 6(64), 59091 (2016)
15. R. S. Singh and A. Solanki, Modulation of electronic properties of silicon carbide nanotubes via sulphur-doping: An *ab initio* study, *Phys. Lett. A* 380(11–12), 1201 (2016)
16. W. Q. Lin, F. Li, G. H. Chen, S. T. Xiao, L. Y. Wang, and Q. Wang, A study on the adsorptions of SO_2 on pristine and phosphorus-doped silicon carbide nanotubes as potential gas sensors, *Ceram. Int.* 46(16), 25171 (2020)
17. Y. Y. Yang, P. Gong, W. D. Ma, R. Hao, and X. Y. Fang, Effects of substitution of group-V atoms for carbon or silicon atoms on optical properties of silicon carbide nanotubes, *Chin. Phys. B* 30(6), 067803 (2021)
18. P. Gong, Y. Y. Yang, W. D. Ma, X. Y. Fang, X. L. Jing, Y. H. Jia, and M. S. Cao, Transport and recombination properties of group-III doped SiCNTs, *Physica E* 128, 114578 (2021)
19. J. M. Zhang, F. L. Zheng, Y. Zhang, and V. Ji, First-principles study on electronic properties of SiC nanoribbon, *J. Mater. Sci.* 45(12), 3259 (2010)
20. Y. Z. Li, M. Y. Sun, X. X. Yu, W. K. Liu, S. S. Kong, Y. L. Li, and X. Y. Fang, First-principles study on optical properties of group-III doped SiCNRs, *Mater. Today Commun.* 32, 104179 (2022)
21. Y. Z. Li, M. Y. Sun, X. X. Yu, W. K. Liu, S. S. Kong, Y. L. Li, and X. Y. Fang, Theoretical study on transport properties of group-III doped SiCNRs, *Eur. Phys. J. Plus* 137(9), 995 (2022)
22. E. Bekaroglu, M. Topsakal, S. Cahangirov, and S. Ciraci, First-principles study of defects and adatoms in silicon carbide honeycomb structures, *Phys. Rev. B* 81(7), 075433 (2010)
23. H. L. Zhu, Z. F. Hong, C. J. Zhou, Q. H. Wu, T. C. Zheng, L. Yang, S. Q. Lan, and W. F. Yang, Energy band alignment of 2D/3D MoS_2/4H-SiC heterostructure modulated by multiple interfacial interactions, *Front. Phys.* 18(1), 13301 (2023)
24. S. S. Lin, Light-emitting two-dimensional ultrathin silicon carbide, *J. Phys. Chem. C* 116(6), 3951 (2012)
25. L. Sun, B. Wang, and Y. Wang, A novel silicon carbide nanosheet for high-performance humidity sensor, *Adv. Mater. Interfaces* 5(6), 1701300 (2018)
26. M. Houmad, O. Dakir, A. Abbassi, A. Benyoussef, A. El Kenz, and H. Ez-Zahraouy, Optical properties of SiC nanosheet, *Optik (Stuttg.)* 127(4), 1867 (2016)
27. X. Lin, S. Lin, Y. Xu, A. A. Hakro, T. Hasan, B. Zhang, B. Yu, J. Luo, E. Li, and H. Chen, *Ab initio* study of electronic and optical behavior of two-dimensional silicon carbide, *J. Mater. Chem. C* 1(11), 2131 (2013)
28. Q. Chen, Y. Jiang, Y. Wang, H. Li, C. Yu, J. Cui, Y. Qin, J. Sun, J. Yan, H. Zheng, D. Chen, J. Wu, Y. Zhang, and Y. Wu, Enhanced supercapacitive performance of novel ultrathin sic nanosheets directly by liquid phase exfoliation, *Inorg. Chem. Commun.* 106(6), 174 (2019)
29. L. Sun, B. Wang, and Y. Wang, High-temperature gas sensor based on novel Pt single atoms@SnO_2 nanorods@SiC nanosheets multi-heterojunctions, *ACS Appl. Mater. Interfaces* 12(19), 21808 (2020)
30. W. K. Liu, S. S. Kong, X. X. Yu, Y. L. Li, L. Z. Yang, Y. Ma, and X. Y. Fang, Interlayer coupling, electronic and optical properties of few-layer silicon carbide nanosheets, *Mater. Today Commun.* 34, 105030 (2023)
31. P. N. Nirmalraj, T. Lutz, S. Kumar, G. S. Duesberg, and J. J. Boland, Nanoscale mapping of electrical resistivity and connectivity in graphene strips and networks, *Nano Lett.* 11(1), 16 (2011)
32. X. Y. Fang, X. X. Yu, H. M. Zheng, H. B. Jin, L. Wang, and M. S. Cao, Temperature-and thickness-dependent electrical conductivity of few-layer graphene and graphene nanosheets, *Phys. Lett. A* 379(37), 2245 (2015)
33. J. Song, H. Liu, and D. J. Henry, Layer effects on electronic structures of multi-walled armchair silicon carbide nanotubes, *Comput. Mater. Sci.* 125, 117 (2016)
34. H. Cheng and J. C. Zheng, Ab initio study of anisotropic mechanical and electronic properties of strained carbon–nitride nanosheet with interlayer bonding, *Front. Phys.* 16(4), 43505 (2021)
35. P. Gong, Y. Z. Li, M. Y. Sun, X. Y. Fang, X. L. Jing, and M. S. Cao, Effect of inter-wall coupling on the electronic structure and optical properties of group-III doped SiCNTs, *Physica B* 620(4), 413276 (2021)
36. J. P. Perdew, K. Burke, and M. Ernzerhof, Generalized gradient approximation made simple, *Phys. Rev. Lett.* 77(18), 3865 (1996)
37. A. Tkatchenko and M. Scheffler, Accurate molecular van der Waals interactions from ground-state electron density and free-atom reference data, *Phys. Rev. Lett.* 102(7), 073005 (2009)
38. Y. Z. Li, M. Y. Sun, X. X. Yu, W. K. Liu, S. S. Kong, P. Gong, and X. Y. Fang, Comparative study on the optical properties of group-V doped SiC nanoribbons, *Mater. Sci. Eng. B* 284, 115896 (2022)
39. M. Y. Sun, Y. Z. Li, X. X. Yu, W. K. Liu, S. S. Kong, P. Gong, and X. Y. Fang, Comparative study on transport and optical properties of silicon carbide nanoribbons with different terminations, *Eur. Phys. J. B* 95(9), 142

(2022)
40. S. Kitipornchai, X. Q. He, and K. M. Liew, Continuum model for the vibration of multilayered graphene sheets, *Phys. Rev. B* 72(7), 075443 (2005)
41. G. Mie, Zur kinetischen theorie der einatomigen Körper, *Ann. Phys.* 316(8), 657 (1903)
42. A. N. Kolmogorov and V. H. Crespi, Smoothest bearings: Interlayer sliding in multiwalled carbon nanotubes, *Phys. Rev. Lett.* 85(22), 4727 (2000)
43. P. Lou and J. Y. Lee, Electrical control of magnetization in narrow zigzag silicon carbon nanoribbons, *J. Phys. Chem. C* 113(50), 21213 (2009)
44. A. N. Kolmogorov and V. H. Crespi, Registry-dependent interlayer potential for graphitic systems, *Phys. Rev. B* 71(23), 235415 (2005)
45. D. L. Wood and J. S. Tauc, Weak absorption tails in amorphous semiconductors, *Phys. Rev. B* 5(8), 3144 (1972)
46. T. Kamiya, S. Aiba, M. Miyakawa, K. Nomura, S. Matsuishi, K. Hayashi, K. Ueda, M. Hirano, and H. Hosono, Field-induced current modulation in nanoporous semiconductor, electron-doped $12CaO{\cdot}7Al_2O_3$, *Chem. Mater.* 17(25), 6311 (2005)
47. W. D. Ma, W. K. Liu, P. Gong, Y. H. Jia, Y. Y. Yang, and X. Y. Fang, Effects of different valence atoms on surface passivation of silicon carbide nanowires, *Int. J. Mod. Phys. B* 35(20), 2150207 (2021)